Spatial properties of soil analyses and airborne measurements for reconnaissance of soil contamination by 137 Cs after Fukushima nuclear accident in 2011

Pedram Masoudi, Mathieu Le Coz, Charlotte Cazala, Kimiaki Saito

Spatial properties of soil analyses and airborne measurements for reconnaissance of soil contamination by ^{137}Cs after Fukushima nuclear accident in 2011

Pedram MASOUDI[1], Mathieu LE COZ[1], Charlotte CAZALA[1*], Kimiaki SAITO[2]

[1] Institut de Radioprotection et de Sûreté Nucléaire (IRSN), PSE-ENV/SEDRE, 31 avenue de la Division Leclerc, 92260 Fontenay-aux-Roses, France

[2] Japan Atomic Energy Agency, 178-4-4 Wakashiba, Kashiwa, Chiba, 227-0871, Japan

* Corresponding author: charlotte.cazala@irsn.fr

HIGHLIGHTS

- Soil analyses and airborne measurements are compared to each other.
- In 47% of cases, both the datasets are compatible in small- and large-dimension variations.
- Despite the general consistency of data, soil analyses are more heterogeneous.
- Spatial-correlation within the variable could be a witness of hotspots in low-contaminated zones.

ABSTRACT

Following Fukushima nuclear disaster, several data gathering campaigns surveyed the radionuclide propagation in the environment. However, the acquired datasets do not have the same sampling dimension. For example, the airborne measurements are some sort of averaging over a circular field of view, beneath the sensor; while the soil analyses are much more punctual. The objective of this work is to compare the soil samples and an airborne survey to investigate whether these two datasets reflect the same spatial patterns or not. This is prerequisite for combining the multiresolution data to create and update the contamination map in a post-accidental situation.

The analyses were performed on square tiles of 20 km side to study large- and small-dimension variations in ^{137}Cs concentration. The former was modelled by fitting a plane (called trend) to the georeferenced data points; and the latter was modelled by computing the difference (called residual) between the trend and the initial data. Dip direction and dip angle of trends as well as minimum spatial correlation distance and anisotropy of residuals were computed for both the soil and airborne datasets and compared. Dip directions are compatible in 73% of the tiles and dip angles are generally close. Anisotropy directions are compatible in 49% of the tiles and minimum spatial correlation distances are significantly more marked for the airborne dataset.

The soil samples and airborne measurements are therefore more in agreement in large-dimension (trend) rather than in small-dimension (residual) variations. More generally, both the datasets allow highlighting the main contamination plumes distinguishable because of high concentration values. The airborne dataset yet appears to be more powerful to quantify spatial correlations, which could be linked to the contamination mechanisms.

1. Introduction

1.1 Post-tsunami nuclear accident

Tohoku-Oki earthquake occurred on Friday 11 March 2011 at 14:46 JST (05:46 UTC). This event with the moment magnitude (M_w) of 9.0 is attributed to the NNE-SSW megathrust where the Pacific Plate subducts below Japan. Despite several tectonic activities in this subduction zone, the magnitude of Tohoku-Oki event is only comparable to Sanriku earthquake on July 15, 1896 (M_w=8.0), occurred ~190 km north east of Tohoku-Oki epicenter. Following the main-shock, several aftershocks (maximum M_w of 7.9) and a tsunami were registered. Although the maximum registered tsunami wave height was 1.9 m (Simons et al., 2011), the wave height of ~15 m was reported at the Fukushima Daiichi Nuclear Power Plant (FDNPP) (IAEA, 2015).

The epicenter of Tohoku-Oki earthquake is ~160 km in the direction of northeast of the FDNPP, of which security system was heavily damaged following this quake, and large amounts of radionuclides were discharged to the environment. The radionuclide propagation occurred in several phases during 14 days with the most significant releases in 15 and 21 March, and finally stopped at 25 March (Katata et al., 2012; Kinoshita et al., 2011).

The released radionuclides were transported mainly in the form of airborne aerosols and deposited on the ground. Then, the deposited radionuclides migrated and disseminated in the environment. The air dose rate distribution due to emitted gamma-rays (photons) of the deposited and migrated radionuclides was characterized and studied (Gonze et al., 2015). More than 99% of the air dose rate is estimated to be originated from the released radiocesium in March 2011 (Saito et al., 2015), and ~22% of the radiocesium is thought to have been deposited on-land in Japan (Morino et al., 2011). Like the Chernobyl disaster, the FDNPP accident is registered as a major stratigraphic event. It is registered in different locations on the earth, close to the accident source (Takahashi et al., 2017) and beyond, e.g. the radionuclide propagation reached Europe seven days after the accident (Masson et al., 2011).

1.2 Radionuclide deposition and redistribution

Released radionuclides on March 15 were the major contributors to the contamination of Fukushima Prefecture, i.e. west of the FDNPP; whereas the discharges of March 21 were mostly deposited south

west of the FDNPP. This observation is related to the meteorological conditions at the time of radionuclides release (Kinoshita et al., 2011). In fact, geometrical shape of the contamination event is controlled not only by the meteorological conditions but also by more complex deposition and redistribution processes.

There are two types of radionuclides deposition: dry and wet deposition. Wind and topography control the former while the latter is controlled by rainfall. Dry deposition contaminates along the passage of plume, close to the release point; the plume flows and widely disperses along the valleys. The rainfall results in more heterogeneous contaminated zones, further from the source of contamination (Katata et al., 2012). The wet deposition is less sensitive to the land-use than the dry deposition (Gonze et al., 2014); and radiation levels are reported to be much less contrasted in the areas dominated by the wet deposits (Gonze et al., 2015). In addition, helicopter surveys revealed that almost all the cesium radionuclides were deposited in the elevations of less than about 1000 m asl (Sanada et al., 2014).

The redistribution processes might decrease the contaminant concentration (radionuclides density) in the soil, meantime increasing it in another environment. The redistribution is either related to natural processes, e.g. rainfall wash-off or radionuclide uptake by the plant roots, or to decontamination activities by the human, e.g. soil removing/ replacing (Gonze et al., 2015). In the Fukushima region, the observed reduction of the air dose rate from June 2011 to December 2012 was 10% higher than physical radioactive decay of the radiocesium, which is attributed to the downward migration in the soil (Andoh et al., 2015; Mikami et al., 2015). Simulations of air dose rate at the flight altitude of 200 m indicated the decrease of ambient dose rate over 12 months: (i) 45% over dense urban areas, (ii) 15% over evergreen coniferous forests and (iii) 2-12% over agricultural lands (Gonze et al., 2016). It means that land-use controls the speed of the natural redistribution processes.

1.3 Surveying the contamination distribution

For observing and characterizing the radionuclide distribution, the operational team of the Aerial Measuring System (AMS) of U.S. Department of Energy (DOE) settled in Japan from 16 March to 28 May 2011. They performed several urgent surveys by fixed-wing aircraft and rotary-wing helicopters (Lyons and Colton, 2012). Many other measurements were also done by different organizations;

however, since they were performed using different methods, it was impossible to integrate these data to create a single distribution map (Mikami et al., 2015).

Therefore, a unified method and protocol for each survey was used during the "National mapping projects", launched on 04 June 2011 by Ministry of Education, Culture, Sports, Science and Technology (MEXT) and commissioned to the Japan Atomic Energy Agency (JAEA) to implement it. The first campaign of the projects comprised systematic soil sampling (lasting about one month) and car-borne surveys, covering wide contaminated areas. Other objectives of the National mapping projects were to securely store the obtained data, to open them to the public, to predict contamination and to simulate migration of radiocesium (Saito and Onda, 2015).

In addition, a series of airborne surveys were conducted till December 2013 by the MEXT. The airborne data (investigation surface of ~300 m) were integrated with the car-borne data (~100 m), using Bayesian kriging, in order to produce the single map of air dose rate (Wainwright et al., 2017).

The current study aims at comparing the soil analyses and the airborne measurements (4^{th} campaign, called airborne#4) from statistical and spatial points of view, in order to investigate whether the soil and the airborne ^{137}Cs (Bq/m^2) datasets are consistent or they reflect different spatial features of the contamination. Answering this question is a prerequisite for combining the multiresolution data to create and update the contamination map, after a nuclear accident.

2. Datasets

Two datasets are investigated in this article: soil analyses and airborne#4 survey. The datasets belong to a semi-circle with a 40 km radius centered at the FDNPP (Fig. 1). Soil analysis were performed on samples taken between 4 June and 8 July 2011 (National mapping project), and the measured ^{137}Cs deposition density was decay-corrected to the reference date of 14 June 2011. Airborne#4 survey was done between 25 October and 5 November 2011, and the ^{137}Cs deposit at the ending date was estimated from the detected gamma-radiation.

2.1 Soil analyses

Soil samples were obtained in over 2000 locations (Fig. 1a), aiming at detecting the regional contamination. Therefore, the locations, where the geographic conditions were expected to change, were

exempted from sampling, e.g. farm fields and riversides. In each location, i.e. a square of the length 3 m, in principle five samples were taken. These five samples are averaged to neutralize the white noise, and to better represent the square of sampling. Therefore one single averaged data is attributed to each sampling location, and the calculations are done on this average value.

The locations were designed following the previous airborne surveys, and the priority was to the habitable areas. There was also a preference to public lands because of the permission issue in the private lands (Onda et al., 2015; Saito et al., 2015). Within the first year after the accident, the contamination was principally limited to the top 2-6 cm of the soil (Fujiwara et al., 2012; Kato et al., 2012; Ohno et al., 2012; Takahashi et al., 2018). Hence, the soil samples belonging to the top 5 cm of the surface layer were collected. Thereafter, the radionuclide concentrations, mostly ^{134}Cs, ^{137}Cs and ^{131}I, were measured by spectrometry systems, calibrated by standard sources of the International Atomic Energy Agency (IAEA) and the Japan Chemical Analysis Center (JCAC) (Saito et al., 2015).

Until the radius of 80 km from the FDNPP, the soil was sampled densely (one sampling location per 2 km^2), and for the distances more than 80 km, one sampling location was designed every 10 km^2 (Saito et al., 2015).

2.2 Airborne measurements

Airborne#4 has scanned the area through the flight lines at ~350 m agl (Fig. 1b). JAEA applied three important transformations to the measurements: (i) altitude correction to 1 m agl; (ii) converting count rates into dose rates; and (iii) converting dose rates into ground deposits. For detailed information about the data acquisition and processing, please refer to the source website at https://emdb.jaea.go.jp/emdb/en/.

The airborne geophysical surveys can investigate only the top soil contamination, i.e. it cannot detect the gamma-rays, emitted from the deep layers. In addition, it is observed that land-use may affect the air dose rate measurement in the higher altitudes, e.g. airborne measurements above forest regions may not be representative of measured air dose rate at ground surface. It is related to the canopy effect and vertical migration of radionuclides through the plants (Gonze et al., 2015).

The airborne measurements are of sort of averaging over a Field Of View (FOV), which is a circular area on the earth, beneath the detector, where the radiation contributes significantly to the recorded

ambient dose rate. Simulations have shown that ~75% of the radiation originates from the horizontal distance of 350 m when radiocesium is exponentially distributed in the ground with a relaxation mass depth of 1 g/cm^2 and the detector is at the height of 300 m (Malins et al., 2015). However, the radius of FOV is recommended to be equal to the height of the detector, here ~350 m, but it could be increased in presence of high energy photo-peaks (Lyons and Colton, 2012).

In the airborne#4, the maximum distance between the flight lines was ~2.5 km. Within each flight line, the measurement was carried out every one second corresponding to the distance of ~40 m.

3. Theories and methods

Spatial variabilities of both the datasets are compared through statistical measures and geostatistical indices. The indices are designed to study different structures of the regional variable. Because the distribution of the studied variable (^{137}Cs deposition density) is lognormal, the measures and indices are applied to $\log_{10}(^{137}\text{Cs})$. Before introducing the measures and indices, the theory of structures of a regional variable is briefly presented.

3.1 Theory of data structures

A regional variable can be decomposed into different structures, with specific bounds of frequency (Matheron, 1982):

$$Z(x) = S_l(x) + S_h(x) + S_n(x) \quad (1)$$

where $Z(x)$ is the regional variable at location x; $S_l(x)$ is the low frequency structure of the regional variable, called "trend"; $S_h(x)$ and $S_n(x)$ are the high frequency structures of the variable, which their summation is called "residual"; and $S_n(x)$ is the noise structure, i.e. high frequency without spatial correlation, while $S_l(x)$ and $S_h(x)$ have spatial correlation.

Trend modelling provides an idea of large-dimension variations and general data orientation. The trend is defined by the scale of study and the objectives. In practice, it could be modelled either by a linear trend or by kriging of the mean of data (Wackernagel, 2003) or by another simple statistical or geometrical model. The trend should be removed from the variable before applying geostatistical analyses, because it might cause the variable to be nonstationary (Gringarten and Deutsch, 2001).

The residual reflects small-dimension variations, which is usually accompanied by the noise. Conventionally, the residual is studied by variography analyses. Considering the residual (R) as a stationary variable, its semi-variogram (γ) could be directionally calculated for different lags (h) (Gringarten and Deutsch, 2001):

$$\gamma(\mathrm{h}) = \frac{1}{2\mathrm{n}} \sum_{i=1}^{n} (R_x - R_{x+h})^2 \quad (2)$$

where n is the number of pair of data with the distance of h; and R_x and R_{x+h} are the residual values at the locations x and x+h, respectively.

3.2 Statistical measures

The study area is 60 by 120 km. Since it is a large area, the analyses are done on a moving square window of the length 20 km, called tile (Fig. 2a). Setting the moving step, i.e. spatial resolution, to 1 km, totally 4141 square tiles were defined. The kernel size was approved after a primary variography analysis on a selection of tiles. It revealed that spatial correlation of $\log_{10}(^{137}\mathrm{Cs})$ is up to 17 km.

For each of the tiles (20 by 20 km), mean and standard deviation of $\log_{10}(^{137}\mathrm{Cs})$ are computed and mapped at the location of the central pixel of the tile (within the mapped zone in Fig. 2a). The standard deviation values are also plotted regarding the mean of $\log_{10}(^{137}\mathrm{Cs})$ for analyzing the heteroscedasticity, i.e. variance variation, of the datasets (Tofallis, 2009).

According to visual evaluation at the scale of 20 km, the trend is nearly always linear, i.e. the trend could be approximated by a plane. Therefore linear regression is used for fitting a plane inside each of the 4141 tiles (Fig. 2b). The plane dip directions are mapped for each dataset, and the plane dip angles are compared where dip directions are consistent. Dip angle represents the slope of the plane, and dip direction represents the azimuth of the slope.

3.3 Geostatistical indices

Following removing the trend, anisotropy and spatial correlation of the residual are studied. For these purposes, experimental semi-variograms are calculated in eight directions in each tile, using geoR open-source R package for geostatistical data analysis. The theoretical background is already explained in the Section 3.1. Then, index of anisotropy and minimum index of spatial correlations are calculated and mapped for every tile of each dataset:

(i) the index of anisotropy is the direction with the minimum average of semi-variogram values, i.e. the direction with the maximum distance of spatial correlation (Fig. 3);

(ii) the index of spatial correlation is the distance at which the semi-variogram reaches the variance of the residual, i.e. firstly a spherical function is fitted to the experimental semi-variogram, then the distance at which the fitted function reaches the variance is determined (Fig. 3).

At the end, the residuals from both the datasets are also compared by the means of correlation coefficient.

4. Results

4.1 Statistical properties

The maps of mean $\log_{10}(^{137}Cs)$ (Fig. 4a, b) show the same plumes of contamination for both the soil and airborne datasets: the first contamination plume is extended from the FDNPP (east of the maps, outside) toward north-west. As the first plume disappears, the second plume appears toward south-west. The southern part of the study area seems to be weakly contaminated. Although the mean values of $\log_{10}(^{137}Cs)$ are highly correlated between soil and airborne datasets (r^2=0.95), airborne mean values are nearly always higher than mean of soil analyses (except in the north western corner where the density of soil sampling locations in the tiles is significantly lower). The former is ~0.20 $\log_{10}(Bq/m^2)$ higher than the latter (Fig. 4c).

The maps of standard deviation of $\log_{10}(^{137}Cs)$ show relatively higher values (~0.014) for the soil analyses, except at the northeast and southeast corners where the airborne standard deviation increases abnormally (Fig. 5a, b). This artifact is explained by the fact that corresponding tiles include the coastline where zero values of airborne data are noticed. Nevertheless, apart from these two corners, the increase of standard deviation could be related to the slopes of the plumes of contamination. Indeed, values are relatively low (i) in the southern part of the study area (less contaminated); (ii) close to the Fukushima City where mean of $\log_{10}(^{137}Cs)$ values are stable in space (~5.2 in Fig. 5c); finally, to a lesser extent (iii) on the axis of the contamination plumes (highly contaminated).

4.2 Trend analyses

The maps of dip direction of linear trend of soil and airborne datasets show similar patterns, especially in the northern part of the study area, where the contamination plumes passed (Fig. 6a, b). The dip directions are compatible for almost 40% of the study area and the difference in dip directions is less than 40° for 76% of the area (Fig. 6c). The difference of dip directions higher than 40° is observed in three areas (Fig. 7a):

(i) A tiny area close to the contamination source at east, i.e. the FDNPP, where 180° change in dip direction occurs in the two datasets. Mean of $\log_{10}(^{137}Cs)$ is the maximum in this area. The cause of this incompatibility might be nonlinear behavior of the data on the axis of the first contamination plume, i.e. the plane is not representative of the data trend.

(ii) The north-western part of the study area, close to Fukushima City, corresponds to a relatively constant contamination: mean is ~5.2 $\log_{10}(Bq/m^2)$, while low standard deviation (Fig. 7b). It means that the trend plane is near horizontal. Therefore, the difference between the dip directions of the soil and airborne datasets is not meaningful.

(iii) In the southern part, neither mean nor standard deviation of $\log_{10}(^{137}Cs)$ is high. This area is less contaminated. In the viewpoint of data structure, the signal to noise ratio is weak, and the radionuclides were not able in constructing spatial correlation. Therefore the dip direction shows random behavior.

The maps of dip angle of the linear trend of both the datasets show similar patterns where dip directions are compatible, i.e. difference of dip directions is less than 40° (Fig. 8a, b). The dip angles of the datasets are well correlated (r^2=0.63) as shown in Fig. 8c. Dip angle of the soil analyses is higher than the airborne measurements, especially in steep angles, and the root mean square difference is 0.79°.

4.3 Residual analyses

The maps of index of anisotropy of both the soil and airborne datasets show some similarities; the soil dataset yet results in a more heterogeneous map (Fig. 9). In 49% of the study area, the difference in anisotropy directions is less than 40°. The main anisotropy directions are estimated to be 157.5° (23% of the study area) and 135° (20% of the study area) for soil analyses and 135° (25% of the study area)

for airborne measurements. The main directions (135° and 157.5°) are distributed principally on the east of the study area, while 22.5° to 67.5° directions dominate the western part.

The maps of minimum index of spatial correlation reveal high spatial correlation distances (>8 km in each tile of 20 km) along the first contamination plume (Fig. 10). Relatively high index values are also noticed on both the maps in a circular zone with 5-10 km diameter in the south of the area. In other locations (65% of the study area), the minimum index of spatial correlation is undetectable in the soil residuals, i.e. the minimum spatial correlation distance falls below the variography lag, which is 2 km; whereas the index varies from 2 to 6 km for the airborne residuals, except in the southwestern part of the area (index undetectable for <17% of the study area).

Correlation coefficient between the residuals of both the datasets is higher than 0.5 in more than half of the area (Fig. 11). It rises as mean of $\log_{10}(^{137}Cs)$ increases. Besides, in areas where the minimum index of spatial correlation is less than 2 km (for the soil dataset), correlation coefficient becomes weaker too.

5. Discussion

Comparing the mean maps reveals that the results from airborne#4 measurements are systematically higher than those from the soil analyses (Fig. 4c). Besides, the maps of dip of linear trend at the slope of plumes indicate steeper descent in the soil analyses, relative to the airborne#4 measurements (Fig. 8). The model of Fig. 12 could thus be proposed for describing behavior of the datasets for high contamination areas; characterizing the contamination by airborne#4 will result in a larger contaminated zone if the same threshold is used on both the datasets, therefore, estimating the contaminated surface by the airborne dataset provides a pessimistic output. This systematic difference between the airborne and the soil datasets could be explained as due to:

(i) the fact that airborne data are geophysical measurements (count rate) at the flight height, which are transformed to the air dose rates at the height of one meter above the ground level, then to the deposition densities; whereas soil data correspond to direct measurement of gamma-ray emission of soil samples;

(ii) the limitations of soil sampling to the bared soil lands and accessible locations (Fig. 13), whereas there is no land-use limitation for airborne measurements; in other language, soil sampling is less representative since it is biased to the accessible locations;

(iii) the possible canopy effect, already introduced in the Section 2.2.

Comparing the residuals of $\log_{10}(^{137}Cs)$ reveals that the related spatial structures have generally the same orientation for both the soil and airborne datasets (Fig. 6). However, the airborne dataset appears to be more suitable for characterizing these spatial structures; indeed, the soil-based experimental semi-variograms are difficult to be interpreted quantitatively due to high variability of soil data between adjacent sampling locations (distances of <2 km, Fig. 10). The observed difference in the residuals might be due to the fact that soil sampling is done in squares of length 3 m, while airborne measurements belong to a FOV of diameter ~700 m. In addition, adjacent airborne measurements along flight-lines show partly the same location, which increases their similarity (Fig. 13) (Masoudi et al., 2017). The soil dataset thus contains higher frequency information that is smoothed in the airborne dataset.

In addition, the maps computed based on residuals show that mechanisms of contamination are very heterogeneous in space. Therefore, a single model of variogram cannot represent the anisotropy and range variations of whole the study area. Hence, for detailed characterization of the contaminated areas, either variograms should be modelled for short distances, e.g. within tiles of 20 km, or variogram-free algorithms, e.g. Multiple Point Statistical algorithms (Le Coz et al., 2011), must be applied.

Finally, this study shows that the area could be categorized and prioritized into three exploratory zones for prospecting the contamination in a nuclear post-accidental situation:

(i) Zone of high priority: highly contaminated zone, easily highlighted based on the mean values.

(ii) Zone of low priority: relatively low contaminated zone but showing high spatial correlation within the variable, characterized through a general trend and/or a marked index of spatial correlation in the residuals. Determining spatially-correlated zones is important since spatial correlation of contamination is a witness of systematic variation of contaminant, i.e. the variation is not perchance, and it is controlled by a mechanism, here radionuclide distribution

and/or redistribution. So, it is probable having contamination concentrations, i.e. hotspots, locally within these zones.

(iii) Zone of non-priority: the low contaminated zone where the trend is poorly defined and the index of spatial correlation in the residuals is low, i.e. the signal to noise ratio is low.

In order to complete this research, all the statistical measures and geostatistical indices were also computed for the ^{134}Cs (soil and airborne#4 datasets). The results and conclusions are very similar to those presented here for the ^{137}Cs.

6. Conclusion

In order to investigate the soil radioactive contamination in a nuclear post-accidental situation, dense coverage of soil sampling is impractical (time consuming, expensive, accessibility limitations and large contaminated surface), however airborne gamma-ray measurement makes a huge volume of data available within some days or a couple of weeks. In this article, it was tried to find out to what extend (and in which aspects) soil and airborne datasets carry the common information. Addressing this problem conducts to better understanding of the datasets, in order to achieve a more accurate contamination characterization.

The importance of soil sampling is inevitable since they are direct and punctual measurements, i.e. each soil analysis represents a small sampled location (9 m^2). However, lack of dense sampling does not permit performing variography analyses, in all the tiles.

On the other hand, airborne measurements benefit from dense sampling in a large region; but the remote detections lack the localization precision, i.e. they are not punctual since measurement takes place over a FOV with the diameter of ~700 m. It is here discussed that dense sampling over FOV results in smoother data with larger variogram range. Hence it is easier to model a semi-variogram for airborne measurements. In addition, in the case of Fukushima post-accidental surveys, the airborne-based cesium deposits are overestimations of soil-based cesium deposits, systematically, which is a big drawback.

Each dataset has its own negative and positive points, and a wise solution to reduce the drawbacks while benefiting of the advantages worth being checked. Since the residuals are correlated, co-kriging algorithms could be used in order to integrate these datasets. Being direct and punctual makes the soil data as a reference of estimation, i.e. the primary variable in the co-kriging algorithm. The airborne data

could be used as secondary variable, which helps in improving the co-variogram (because of good coverage and high spatial correlation).

Finally, based on the reconnaissance phase, it is also recommended to perform detailed characterization within the square tiles of 20 km. In this dimension, variography analysis would be conformable because anisotropy is often unchanged within 20 km. The other recommendation is that linear regression is not the best choice for trend modelling in whole the area. Specifically close to the plumes axis, it is suggested therefore to model the trend, nonlinearly.

Acknowledgements and disclaim

The study has been conducted in the context of the TERRITORIES project, which is part of the EJP CONCERT, funded from the Euratom research and training program 2014-2018 under grant agreement No 662287. The authors are thankful to Japanese Atomic Energy Agency (JAEA) for permitting the use of their data and publication of scientific results. Christelle Courbet is acknowledged for launching this research project in the IRSN. Finally, the authors would like to thank Marc-André Gonze, researcher of the LEREN laboratory at IRSN and the members of the LTD laboratory at IRSN for their comments and advices during the project.

This publication reflects only the author's view. Responsibility for the information and views expressed therein lies entirely with the authors. The European Commission is not responsible for any use that may be made of the information it contains.

References

Andoh, M., Nakahara, Y., Tsuda, S., Yoshida, T., Matsuda, N., Takahashi, F., Mikami, S., Kinouchi, N., Sato, T., Tanigaki, M., Takamiya, K., Sato, N., Okumura, R., Uchihori, Y., Saito, K., 2015. Measurement of air dose rates over a wide area around the Fukushima Dai-ichi Nuclear Power Plant through a series of car-borne surveys. J. Environ. Radioact. 139, 266–280. doi:10.1016/j.jenvrad.2014.05.014

Fujiwara, T., Saito, T., Muroya, Y., Sawahata, H., Yamashita, Y., Nagasaki, S., Okamoto, K., Takahashi, H., Uesaka, M., Katsumura, Y., Tanaka, S., 2012. Isotopic ratio and vertical distribution of radionuclides in soil affected by the accident of Fukushima Dai-Ichi nuclear power plants. J. Environ. Radioact. 113, 37–44. doi:10.1016/j.jenvrad.2012.04.007

Gonze, M.A., Mourlon, C., Calmon, P., Manach, E., Debayle, C., Baccou, J., 2016. Modelling the dynamics of ambient dose rates induced by radiocaesium in the Fukushima terrestrial environment. J. Environ. Radioact. 161, 22–34. doi:10.1016/j.jenvrad.2015.06.003

Gonze, M.A., Mourlon, C., Calmon, P., Manach, E., Debayle, C., Gurriaran, R., Baccou, J., 2015. Assessment study of ambient dose rates dynamics in the Fukushima terrestrial region, in: The 7thEuropean Review Meeting on Severe Accident Research (ERMSAR-2015). Marseille, pp. 24–26.

Gonze, M.A., Renaud, P., Korsakissok, I., Kato, H., Hinton, T.G., Mourlon, C., Simon-Cornu, M., 2014. Assessment of dry and wet atmospheric deposits of radioactive aerosols: Application to Fukushima radiocaesium fallout. Environ. Sci. Technol. 48, 11268–11276. doi:10.1021/es502590s

Gringarten, E., Deutsch, C. V, 2001. Teacher's aide variogram interpretation and modeling. Math. Geol. 33, 507–534. doi:10.1023/a:1011093014141

IAEA, 2015. The Fukushima Daiichi accident report by the director general, International Atomic Energy Agency. Vienna.

Katata, G., Terada, H., Nagai, H., Chino, M., 2012. Numerical reconstruction of high dose rate zones due to the Fukushima Dai-ichi Nuclear Power Plant accident. J. Environ. Radioact. 111, 2–12. doi:10.1016/j.jenvrad.2011.09.011

Kato, H., Onda, Y., Teramage, M., 2012. Depth distribution of 137Cs, 134Cs, and 131I in soil profile after Fukushima Dai-ichi Nuclear Power Plant Accident. J. Environ. Radioact. 111, 59–64. doi:10.1016/j.jenvrad.2011.10.003

Kinoshita, N., Sueki, K., Sasa, K., Kitagawa, J. -i., Ikarashi, S., Nishimura, T., Wong, Y.-S., Satou, Y., Handa, K., Takahashi, T., Sato, M., Yamagata, T., 2011. Assessment of individual radionuclide distributions from the Fukushima nuclear accident covering central-east Japan. Proc. Natl. Acad. Sci. doi:10.1073/pnas.1111724108

Le Coz, M., Genthon, P., Adler, P.M., 2011. Multiple-point statistics for modeling facies heterogeneities in a porous medium: The Komadugu-Yobe alluvium, Lake Chad basin. Math. Geosci. 43, 861.

Lyons, C., Colton, D., 2012. Aerial measuring system in Japan. Health Phys. 102, 509–515. doi:10.1097/HP.0b013e31824d0056

Malins, A., Okumura, M., Machida, M., Takemiya, H., Saito, K., 2015. Fields of view for environmental radioactivity, in: The International Symposium on Radiological Issues for Fukushima's Revitalized Future. pp. 28–34.

Masoudi, P., Memarian, H., Aïfa, T., Tokhmechi, B., 2017. Geometric modelling of the volume of investigation of well logs for thin-bed characterization. J. Geophys. Eng. 14, 426–444. doi:10.1088/1742-2140/aa59d4

Masson, O., Baeza, A., Bieringer, J., Brudecki, K., Bucci, S., Cappai, M., Carvalho, F.P., Connan, O., Cosma, C., Dalheimer, A., 2011. Tracking of airborne radionuclides from the damaged Fukushima Dai-ichi Nuclear Reactors by European Networks. Environ. Sci. Technol. 45, 7670–7677.

Matheron, G., 1982. Pour une analyse krigeante des données regionalisées, Tech. Rep. N-732. Fontainebleau.

Mikami, S., Maeyama, T., Hoshide, Y., Sakamoto, R., Sato, S., Okuda, N., Sato, T., Takemiya, H., Saito, K., 2015. The air dose rate around the Fukushima Dai-ichi Nuclear Power Plant: Its spatial characteristics and temporal changes until December 2012. J. Environ. Radioact. 139, 250–259. doi:10.1016/j.jenvrad.2014.08.020

Morino, Y., Ohara, T., Nishizawa, M., 2011. Atmospheric behavior, deposition, and budget of radioactive materials from the Fukushima Daiichi nuclear power plant in March 2011. Geophys. Res. Lett. doi:10.1029/2011GL048689

Ohno, T., Muramatsu, Y., Miura, Y., Oda, K., Inagawa, N., Ogawa, H., Yamazaki, A., Toyama, C., Sato, M., 2012. Depth profiles of radioactive cesium and iodine released from the Fukushima Daiichi nuclear power plant in different agricultural fields and forests. Geochem. J. 46, 287–295. doi:10.2343/geochemj.2.0204

Onda, Y., Kato, H., Hoshi, M., Takahashi, Y., Nguyen, M.L., 2015. Soil sampling and analytical strategies for mapping fallout in nuclear emergencies based on the Fukushima Dai-ichi Nuclear Power Plant accident. J. Environ. Radioact. 139, 300–307. doi:10.1016/j.jenvrad.2014.06.002

Saito, K., Onda, Y., 2015. Outline of the national mapping projects implemented after the Fukushima accident. J. Environ. Radioact. 139, 240–249. doi:10.1016/j.jenvrad.2014.10.009

Saito, K., Tanihata, I., Fujiwara, M., Saito, T., Shimoura, S., Otsuka, T., Onda, Y., Hoshi, M., Ikeuchi, Y., Takahashi, F., Kinouchi, N., Saegusa, J., Seki, A., Takemiya, H., Shibata, T., 2015. Detailed deposition density maps constructed by large-scale soil sampling for gamma-ray emitting radioactive nuclides from the Fukushima Dai-ichi Nuclear Power Plant accident. J. Environ. Radioact. 139, 308–319. doi:10.1016/j.jenvrad.2014.02.014

Sanada, Y., Sugita, T., Nishizawa, Y., Kondo, A., Torii, T., 2014. The aerial radiation monitoring in Japan after the Fukushima Daiichi nuclear power plant accident. Prog. Nucl. Sci. Technol. 4, 76–

80. doi:10.15669/pnst.4.76
Simons, M., Minson, S.E., Sladen, A., Ortega, F., Jiang, J., Owen, S.E., Meng, L., Ampuero, J.-P., Wei, S., Chu, R., Helmberger, D. V, Kanamori, H., Hetland, E., Moore, A.W., Webb, F.H., 2011. The 2011 magnitude 9.0 Tohoku-Oki earthquake: Mosaicking the megathrust from seconds to centuries. Science (80-.). 332, 1421 LP-1425.
Takahashi, J., Wakabayashi, S., Tamura, K., Onda, Y., 2018. Downward migration of radiocesium in an abandoned paddy soil after the Fukushima Dai-ichi Nuclear Power Plant accident. J. Environ. Radioact. 182, 157–164. doi:10.1016/j.jenvrad.2017.11.034
Takahashi, Y., Fan, Q., Suga, H., Tanaka, K., Sakaguchi, A., Takeichi, Y., Ono, K., Mase, K., Kato, K., Kanivets, V. V., 2017. Comparison of solid-water partitions of radiocesium in river waters in Fukushima and Chernobyl areas. Sci. Rep. 7, 1–11. doi:10.1038/s41598-017-12391-7
Tofallis, C., 2009. Least squares percentage regression. J. Mod. Appl. Stat. Methods 1–12. doi:10.2139/ssrn.1406472
Wackernagel, H., 2003. Multivariate geostatistics: an introduction with applications, 3rd ed. Springer-Verlag Berlin Heidelberg GmbH, Heidelberg. doi:10.1007/978-3-662-05294-5
Wainwright, H.M., Seki, A., Chen, J., Saito, K., 2017. A multiscale Bayesian data integration approach for mapping air dose rates around the Fukushima Daiichi Nuclear Power Plant. J. Environ. Radioact. 167, 62–69. doi:10.1016/j.jenvrad.2016.11.033

Figures

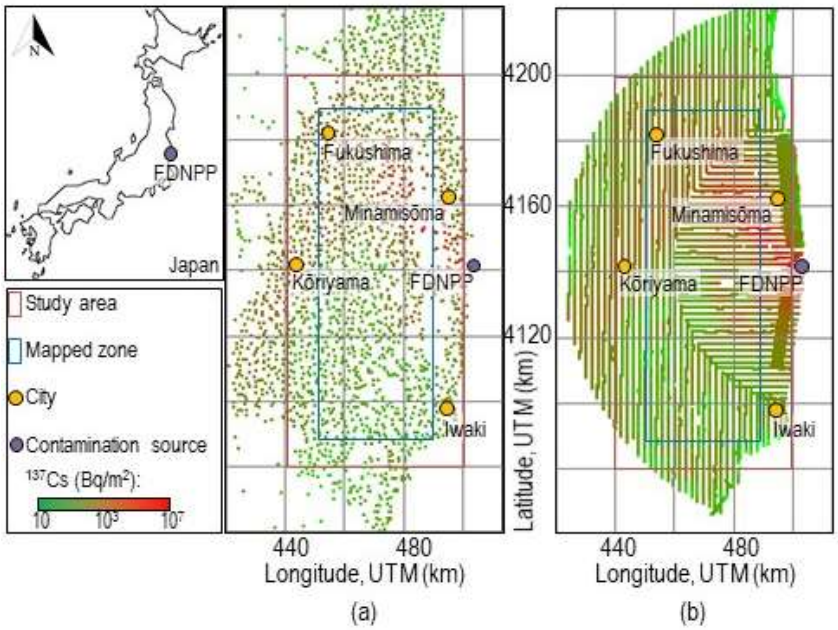

Fig. 1. Location maps of soil sampling (a) and airborne#4 measurements (b).

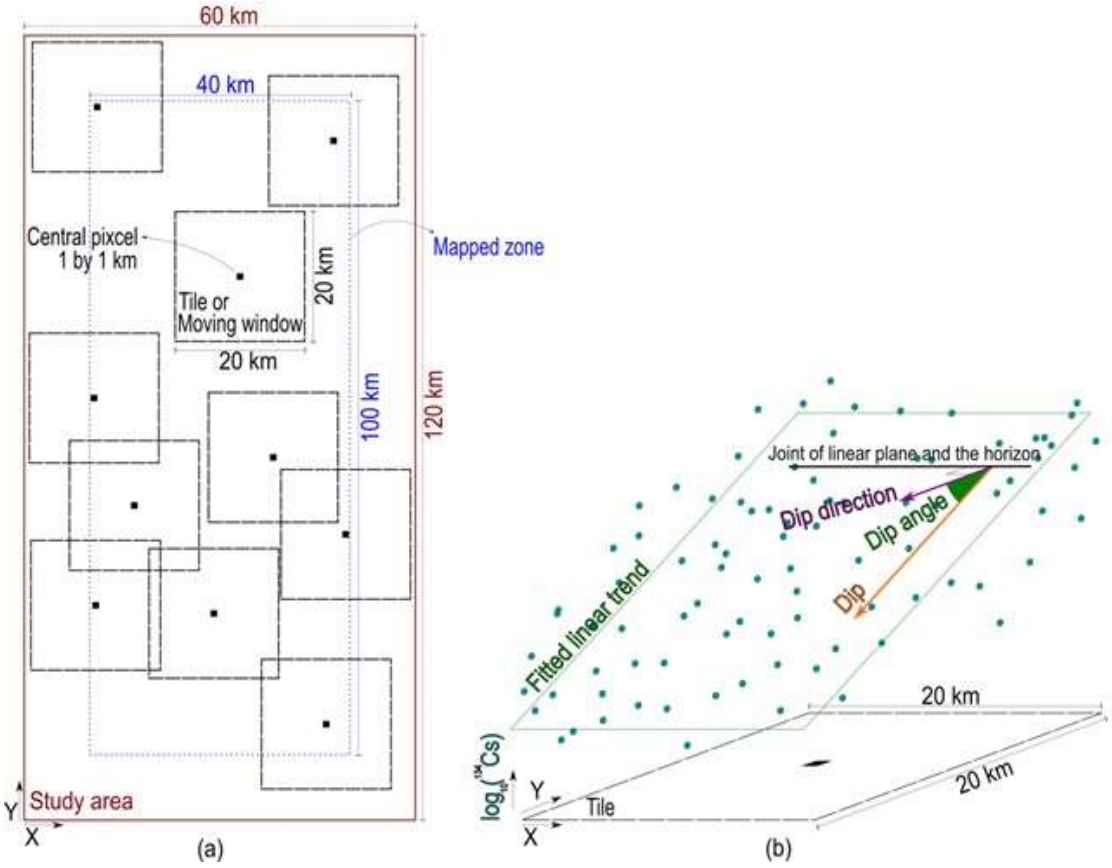

Fig. 2. Schematic representation of the tile (or moving window) on the study area (a). The calculated measures and indices in each tile are visualized at the central pixel, shown in black. Statistical measures (b). Fitted linear trend is a linear regression between $\log_{10}(^{137}Cs)$ and the coordination system, in each tile. Dip direction is a horizontal vector, perpendicular to the joint of the linear trend and the horizontal plane. Dip is a vector parallel to the linear trend and perpendicular to its joint with the horizontal plane. Finally, dip angle is the angle between dip direction and dip angle.

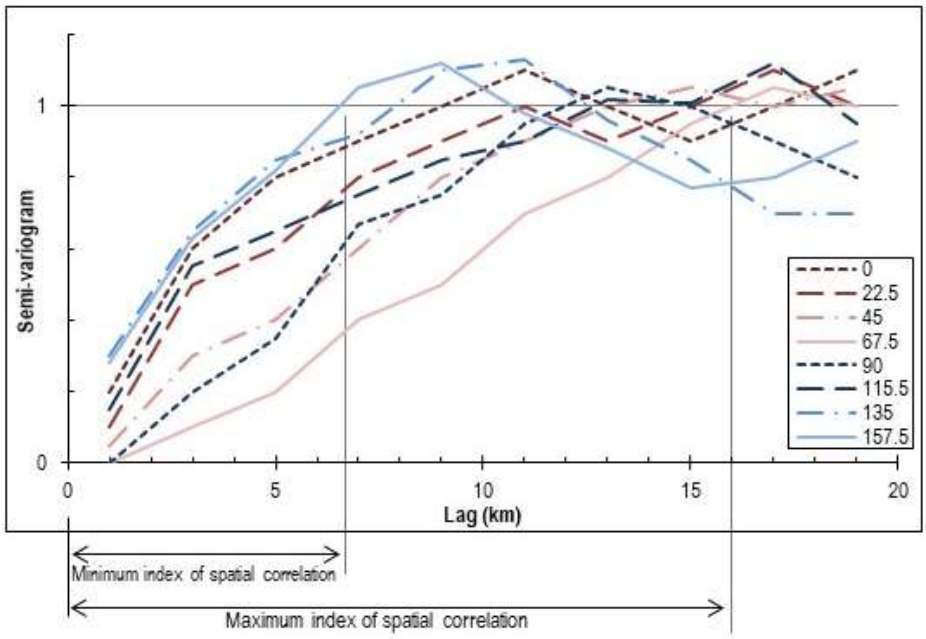

Fig. 3. Schematic representation of experimental semi-variograms in eight directions. Legend is in degree, 0^{o} is toward the north. The indices of spatial correlation are shown accordingly. In this example, direction 67.5^{o} corresponds to the defined index of anisotropy.

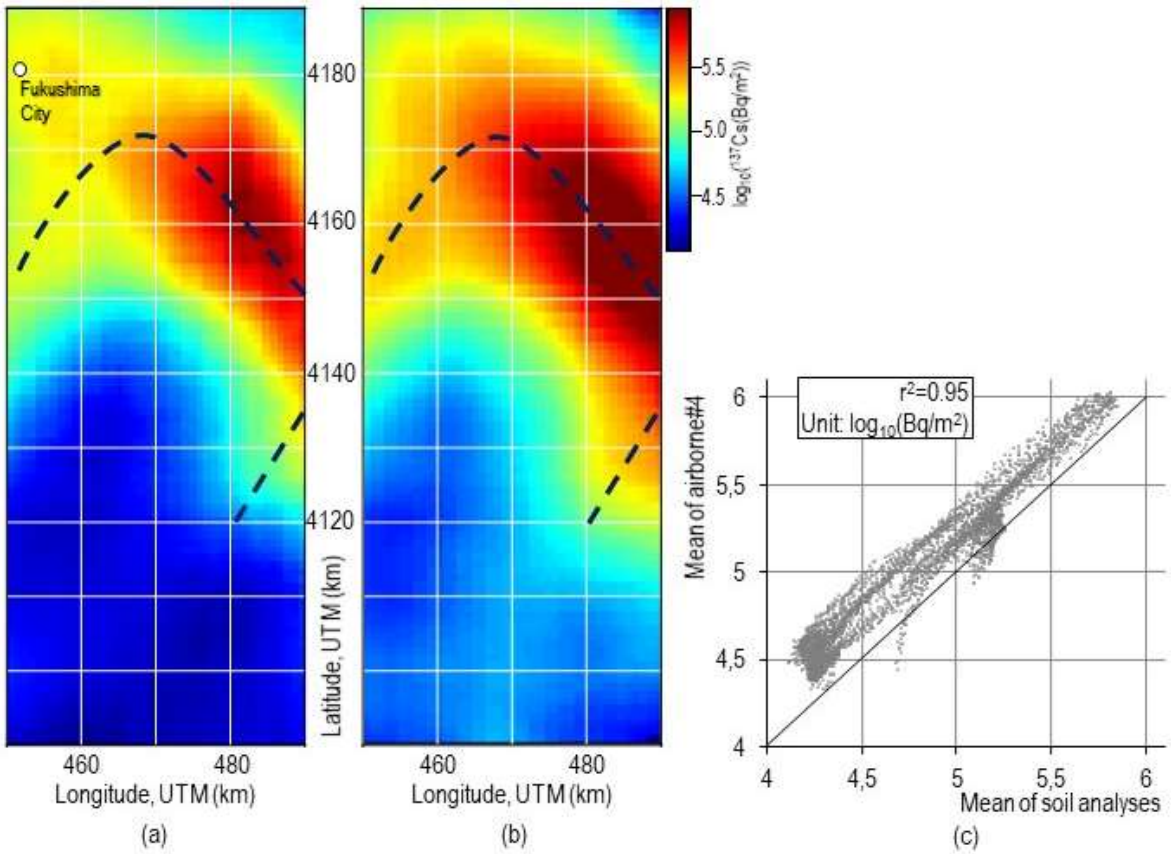

Fig. 4. Mean of $\log_{10}(^{137}Cs)$ for soil analyses (a) and airborne#4 measurements (b) in 4141 tiles, and their cross-plot (c). The cross-plot axes are in the same unit as the color-bar. The dashed-lines on the maps (a and b) indicate the axes of contamination plumes.

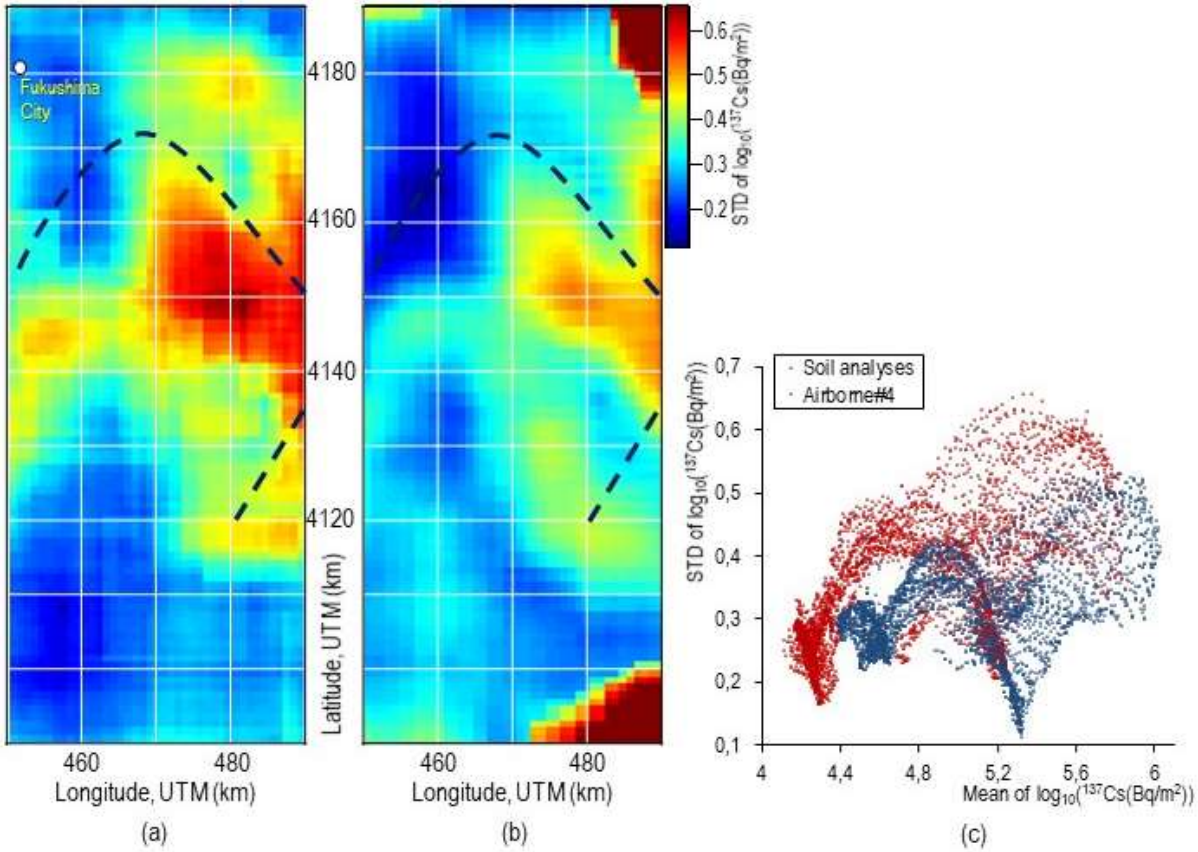

Fig. 5. Standard deviation (STD) of $\log_{10}(^{137}Cs)$ for soil analyses (a) and airborne#4 measurements (b), and their cross-plots of versus the mean of $\log_{10}(^{137}Cs)$ (c). The dashed-lines on the maps (a and b) indicate the axes of contamination plumes.

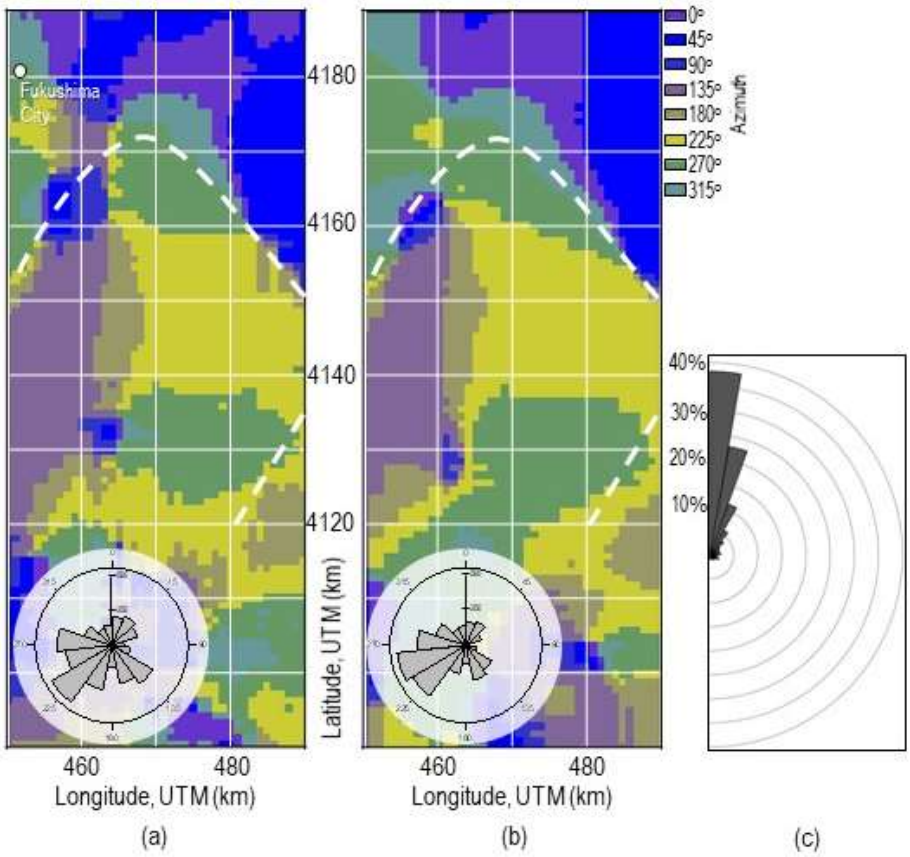

Fig. 6. Dip direction of planar trend of soil analyses (a) and airborne#4 measurements (b). The small rose diagrams on the bottom-left of the maps are azimuthal histograms. The difference between dip direction of planar trends of soil and airborne data is represented by azimuthal PDF rose diagram (c). Each bin of rose diagram corresponds to 10°. The dashed-lines on the maps (a and b) indicate the axes of contamination plumes.

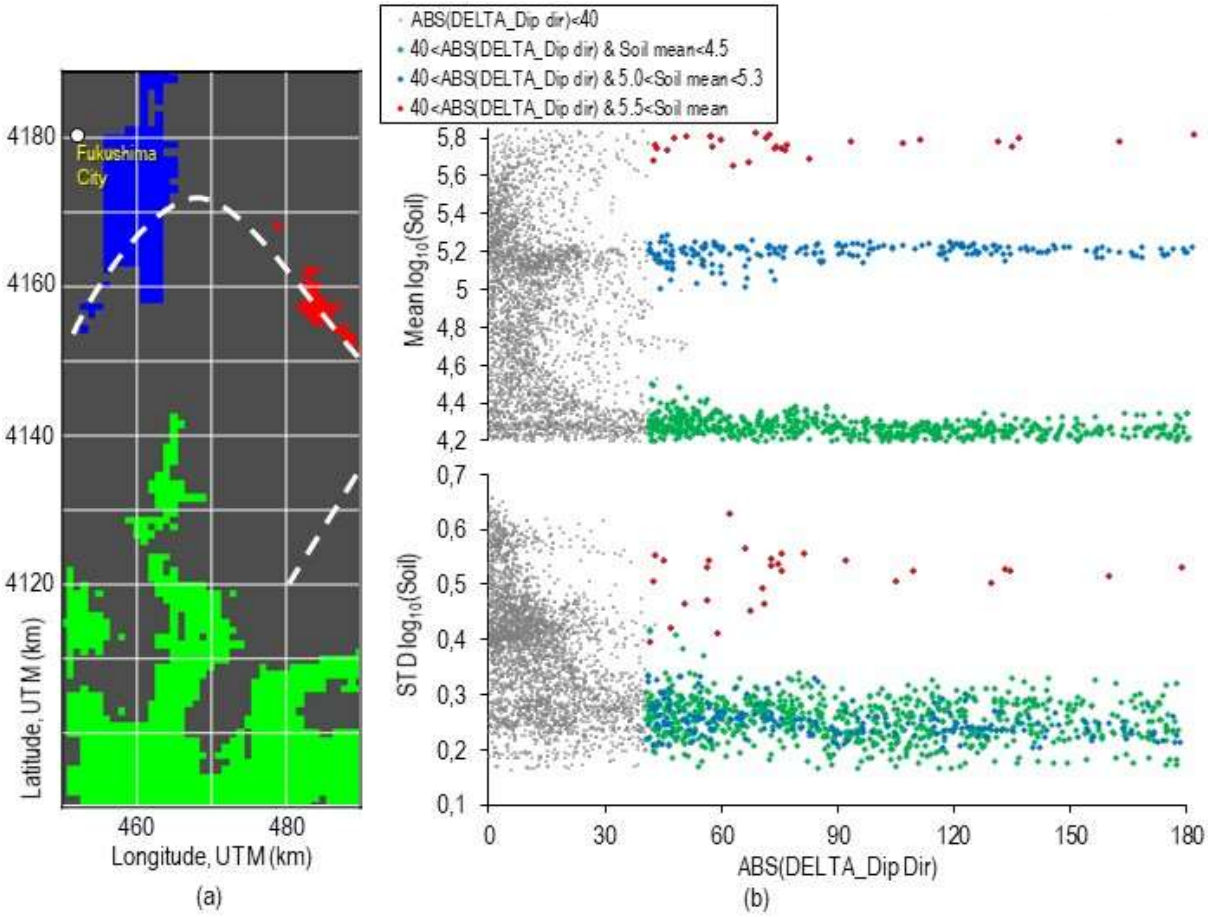

Fig. 7. Areas (colored) where the trends of soil and airborne datasets are incompatible (a). Highlighting the corresponding mean and standard deviation of soil dataset in each tile (b): ABS(DELTA_Dip dir) means the absolute difference of dip direction, the units are the same as Fig. 5c. The dashed-lines on the map (a) indicate the axes of contamination plumes.

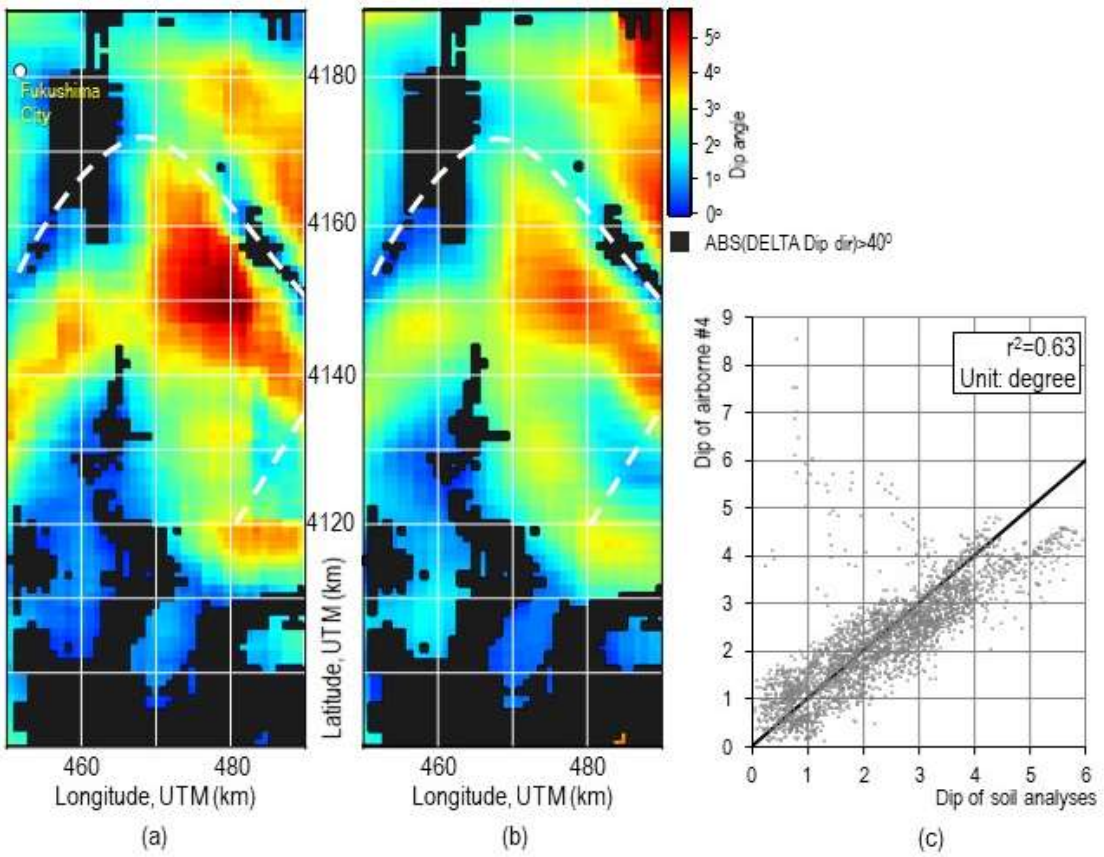

Fig. 8. Dip angle of planar trend of soil (a) and airborne#4 measurements (b) datasets, when the absolute difference of dip direction of trend is less than 40°. The cross-plot of the dips (c). The dashed-lines on the maps (a and b) indicate the axes of contamination plumes.

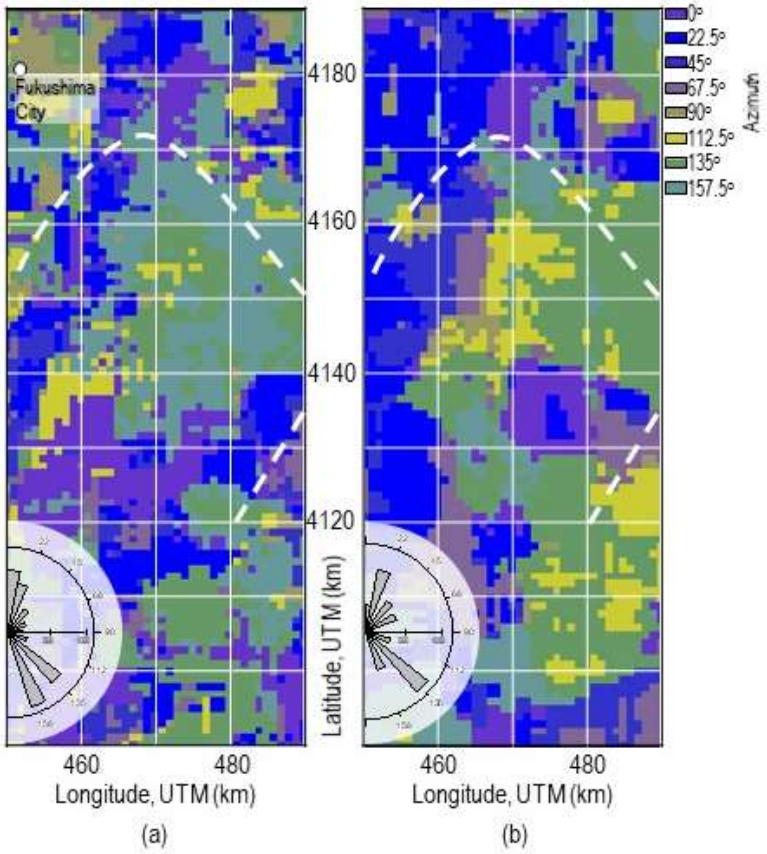

Fig. 9. Index of anisotropy, applied to the residuals of soil (a) and airborne#4 measurements (b) datasets. The dashed-lines on the maps indicate the axes of contamination plumes. The small rose diagrams on the bottom-left of the maps are azimuthal histograms.

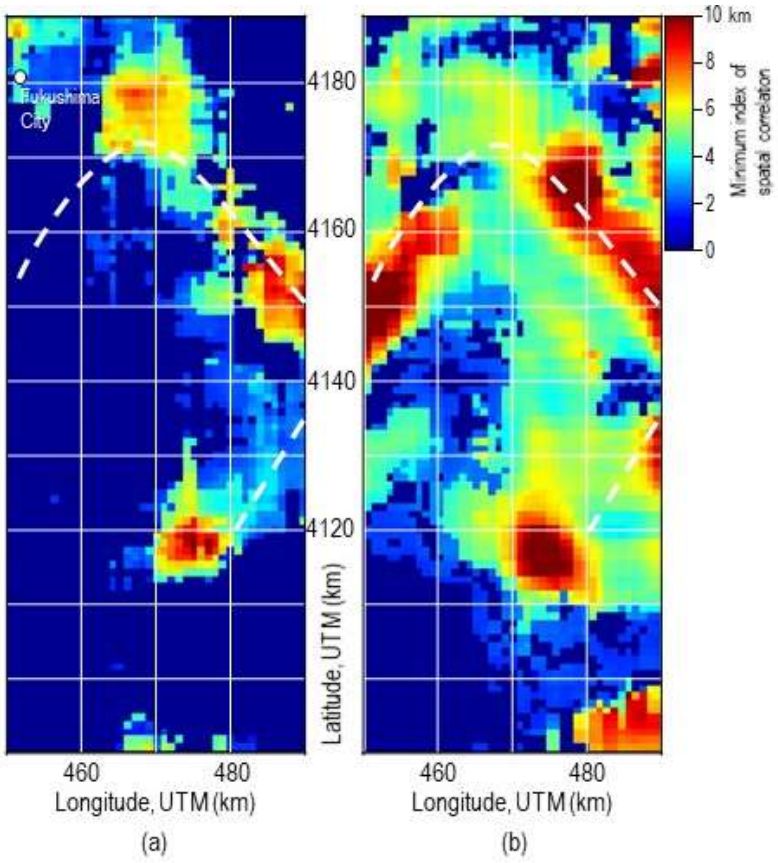

Fig. 10. Minimum index of spatial correlation, applied to the residuals of soil (a) and airborne#4 measurements (b) datasets. The dashed-lines indicate the axes of contamination plumes.

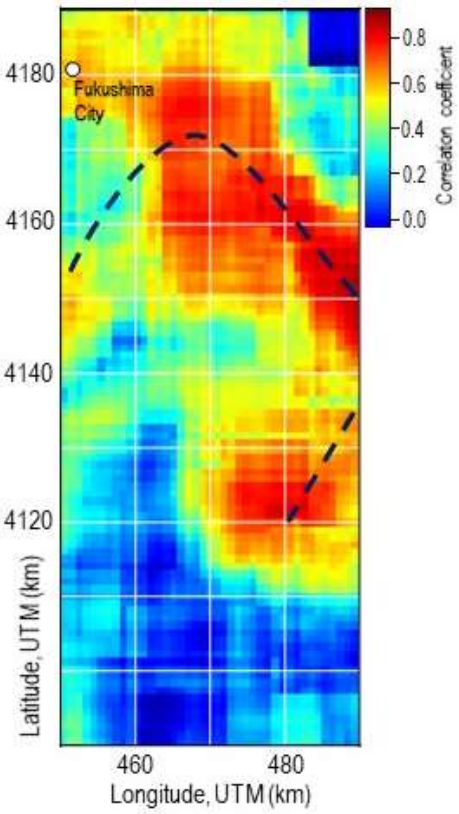

Fig. 11. Correlation coefficient between the residuals of soil analyses and airborne#4 measurements. The dashed-lines indicate the axes of contamination plumes.

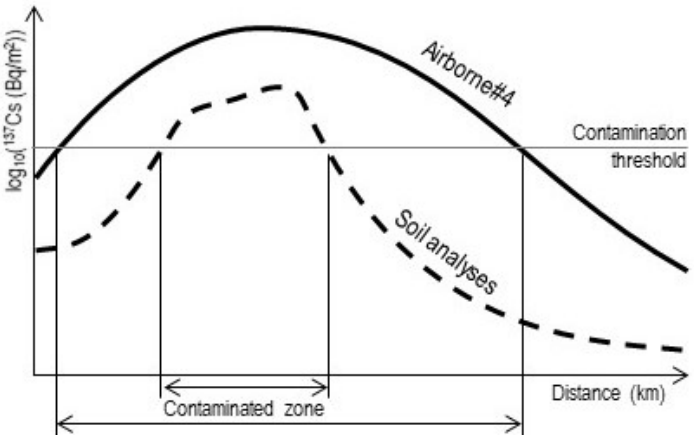

Fig. 12. Proposed model of $\log_{10}(^{137}Cs)$ contamination in the soil analyses and airborne#4 measurements: relatively higher airborne values, sharper slope of the soil dataset, which is also more heterogeneous.

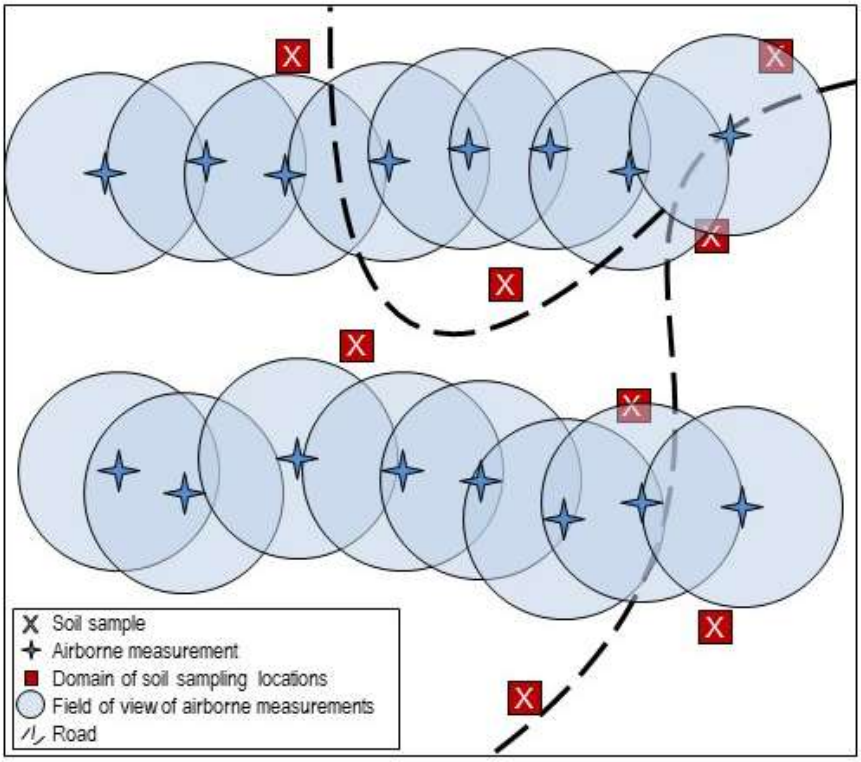

Fig. 13. Schematic of sampling patterns. Soil analyses locations are distributed in the accessible area, e.g. close to the roads, while airborne measurements are aligned. In addition, airborne measurements are denser parallel to the flight lines, whereas soil sampling locations are distributed in an isotropic pattern. The soil analyses belong to a much smaller domain, compared to the field of view of airborne measurements.